Chem Soc Rev

TUTORIAL REVIEW

View Article Online
View Journal | View Issue

Published on 12 April 2018. Downloaded by University of Illinois at Chicago on 8/23/2018 9:50:25 PM.

Check for updates

Cite this: *Chem. Soc. Rev.*, 2018, **47**, 3849

Computational studies of micellar and nanoparticle nanomedicines

Soumyo Sen,[a] Yanxiao Han,[a] Pavel Rehak,[a] Lela Vuković *[b] and Petr Král *[acd]

Received 9th January 2018

DOI: 10.1039/c8cs00022k

rsc.li/chem-soc-rev

Nanomedicines are typically formed by nanocarriers which can deliver in a targeted manner drugs poorly soluble in blood, increase their therapeutic activities, and reduce their side effects. Many tested nanomedicines are formed by lipids, polymers, and other amphiphilic molecules isolated or self-assembled into various complexes and micelles, functionalized nanoparticles, and other bio-compatible composite materials. Here, we show how atomistic molecular dynamics simulations can be used to characterize and optimize the structure, stability, and activity of selected nanomedicines. We discuss modeling of nanomedicines based on micelles, which can deliver selected therapeutic agents, and nanoparticles designed to act like large drugs. We show how to model nanomedicines interacting with lipid membranes, viruses, and amyloid fibrils.

Key learning points

1. Modeling of micellar nanomedicines: design and optimization, drug solvation, role of branched monomers, interactions with membranes and receptors, protein corona.
2. Modeling of nanoparticle nanomedicines: protein adsorption, enzymatic complexes, multivalent blocking of active sites, virus disassembly.

1 Introduction

Numerous modern drugs are poorly soluble in blood.[1] Therefore, many types of nanocarriers have been designed to encapsulate such drugs in their hydrophobic interior,[2] protect them from degradation,[3] selectively deliver them to diseased sites while reducing their negative side-effects through passive or active targeting,[4] and greatly improve the efficacy of treatment.[5]

Micelles are an excellent example of a highly successful nanocarrier platform which can be used to deliver drugs.[6] Micelles can be formed by amphiphilic copolymers of different architectures and chemistries, which tend to self-assemble above a critical micelle concentration (CMC) into complexes of an aggregation number N_{agg}. Typically, hydrophobic blocks of these copolymers are present in the micelle core, while the hydrophilic blocks are exposed to the aqueous solvent.[7] Hydrophobic drugs could be solvated in the micelle core, while the copolymer blocks exposed to the solvent can be functionalized to actively target preferred biomolecules at disease sites, where the carried drugs can be released.[8] However, the exact structure and activity of these nanomedicines are often unclear from the experiments. Precise modeling could clarify where in the micelles, how, and how many drugs are attached, carried, and delivered.

Nanomedicines can also be based on bio-active polymers, molecular complexes, clusters, and nanoparticles (NPs), which can either carry drugs or be designed to act like drugs. In drug-less nanomedicines, it might be difficult to understand from the experiments the concerted activity of different NPs groups during their active binding to selective molecular targets. For all these reasons, precise modeling methods would be useful in designing and optimizing of nanomedicines.

Although many experimental methods have been used to characterize physical and pharmaceutical properties of the prepared nanomedicines,[9] they have been precisely modeled only in a very limited way,[10,11] except DNA-delivery systems.[12] Yet, the large computational power currently available provides many possibilities for precise modeling of biomedical systems.[13] Atomistic molecular dynamics (MD) simulations, today routinely performed for very large biological systems, could be used to better understand nanomedicines and guide their optimal design.

In this tutorial review, we discuss atomistic MD simulations of nanomedicines based on micellar drug nanocarriers and bio-active nanoparticles. First, modeling of micellar nanomedicines

[a] *Department of Chemistry, University of Illinois at Chicago, Chicago, IL, USA. E-mail: pkral@uic.edu*
[b] *Department of Chemistry and Biochemistry, University of Texas at El Paso, El Paso, TX, USA. E-mail: lvukovic@utep.edu*
[c] *Department of Physics, University of Illinois at Chicago, Chicago, IL, USA*
[d] *Department of Pharmaceutical Sciences, University of Illinois at Chicago, Chicago, IL, USA*

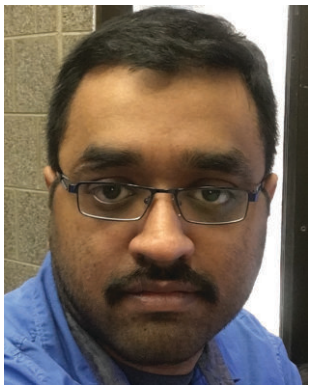
Published on 12 April 2018. Downloaded by University of Illinois at Chicago on 8/23/2018 9:50:25 PM.

is discussed, with a focus on their design and optimization, drug solvation, role of branched monomers, interactions with membranes and receptors, and protein corona. Second, modeling of NPs nanomedicines is discussed, with a focus on their protein adsorption, enzymatic activity, multivalent blocking of active sites, and destabilization of viruses and fibrils.

2 Simulation methods

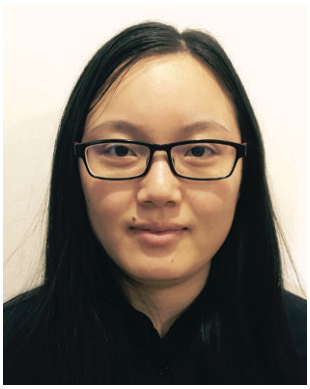
All the systems discussed in this review were studied by classical atomistic MD simulations. The initial structures of micellar and nanoparticle nanomedicines were prepared with GaussView (small molecules), VMD[14] (biomolecules), customized codes (micelles and NPs), and CHARMM-GUI interface (lipids). The initial structures of small molecules, lipids, polymers and NPs were built based on chemical intuition, since they were able to relax into their energy minimum structures on the simulation timescales (10–100s of nanoseconds). The initial structures of proteins and nucleic acids were prepared based on their crystal structures, obtained from the PDB database. When necessary, the Modeller program was used to add unresolved (missing) protein residues in the crystal structures. The complete systems were solvated and ionized by VMD,[14] in order to mimic the experimental conditions.

Atomistic MD simulations of the prepared systems were carried out with the NAMD2 software.[15] All the systems were described with the appropriate CHARMM forcefield (proteins, nucleic acids, lipids) or a general force field;[16] a straightforward automated procedure can be employed for the addition of parameters for new molecules into CHARMM forcefield, which is often required for modeling of nanomedicines and nanoparticles with diverse chemistries.[17] After a quick initial energy minimization and warming to the desired temperature ($<10\,000$ steps), water and ions were equilibrated around the restrained systems for ≈ 2 ns. Then, production run simulations



Soumyo Sen

Soumyo Sen received his BSc in chemistry from the Jadavpur University, Kolkata, India in 2009 and his MSc degree in 2011 from the Indian Institute of Technology, Madras (IITM), India. Then, he worked for a year as a research assistant in Prof. Sanjib Senapati's group in the Biotechnology Department of IITM, where he studied electronic structures of silver nanoclusters. In 2012, he started his PhD studies in the Prof. Petr Král's group at the University of Illinois at Chicago. In 2018, he should defend his PhD thesis devoted to multiscale modeling of nanoparticles growth, self-assembly and applications in nanomedicines.



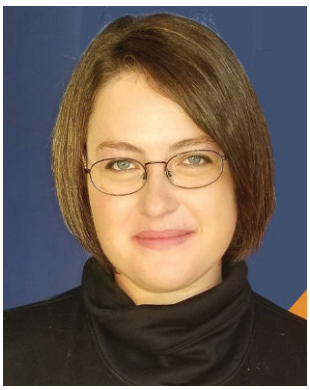
Yanxiao Han

Yanxiao Han received her BS from Ludong University in China in 2012. She then joined the Chuan-Lu Yang research group at Ludong University and obtained her Master's degree in atomic and molecular physics in 2015. In 2015, she started her PhD studies in the Prof. Petr Král's group at the University of Illinois at Chicago. Her research is focused on molecular dynamic simulations of bio-related systems and self-assembly of nanoscale systems.



Pavel Rehak

Pavel L. Rehak received his BSc degree in chemistry and mathematics at the State University of New York at Stony Brook in 2010. He received his MSc in chemical physics at the University of Minnesota Twin Cities in 2012. Then, he continued in developing hybrid QM–MM methods using ionic liquids. In 2015, he started his PhD studies in the Prof. Petr Král's group at the University of Illinois at Chicago. His research involves nanoscale simulations with applications in biochemistry, pharmaceutics, and material sciences.



Lela Vuković

Prof. Lela Vuković received her BSc (2005) and PhD (2012) degrees from the University of Illinois at Chicago, last in the group of Prof. Petr Král. In 2011–2012, she was a visiting researcher in the Max Planck Institute for Biophysical Chemistry. In 2012–2015, she was a postdoctoral fellow of the NSF Center for Living Cells at the University of Illinois at Urbana-Champaign, working with Prof. Klaus Schulten. In 2016, she joined the faculty of the University of Texas at El Paso, as an Assistant Professor. Her current research interests include computational modeling of materials and biomolecular complexes.

 This journal is © The Royal Society of Chemistry 2018

Published on 12 April 2018. Downloaded by University of Illinois at Chicago on 8/23/2018 9:50:25 PM.

were carried out, in which the whole systems were equilibrated on the timescales of 10–100s nanoseconds. These simulations were typically performed in the *NPT* ensemble (P = 1 bar and T = 300 K) with periodic boundary conditions, where pressure and temperature were maintained using a modified Nose–Hoover method with Langevin dynamics. The timestep was set to 2 fs, and long-range interactions were evaluated every 1 (van der Waals) and 2 timesteps (Coulombic); the particle-mesh Ewald method was used for the evaluation of long-range Coulomb interactions.

Several studies discussed below evaluated also the free energies of binding. Methods based on a potential of mean force, including an adaptive biasing force method and an umbrella sampling method, were used to determine free energy profiles with respect to intermolecular distances.

3 Linear copolymer micelles

In the early studies, only rather small systems were modeled, such as the self-assembly of small dodecylphosphocholine surfactant micelles.[18] Recently, atomistic MD simulations were employed to characterize micelles assembled from charged DSPE-PEG_{2000} (1,2-distearoyl-*sn-glycero*-3-phosphatidylethanolamine-*N*-[methoxy(polyethyleneglycol) 2000]) copolymers, as shown in Fig. 1(A). These FDA-approved PEG-ylated nanocarriers, called sterically stabilized micelles (SSM), can serve as platforms for association of both hydrophobic and amphiphilic drugs and peptides.[19]

Dynamic light scattering studies revealed that the sizes of experimentally prepared DSPE-PEG_{2000} assemblies depend on the ionic strength of the aqueous solution. The average DSPE-PEG_{2000} micelle diameters (at 5 mM monomer concentration) were ≈5 nm in pure water and ≈15 nm in saline solution (0.16 M NaCl, representative of physiological conditions), as seen in Fig. 1(B). The sizes of nanocarriers can affect their toxicity and tissue-permeability, while their stability is key to regulating their residence time in the bloodstream and the drug release kinetics.

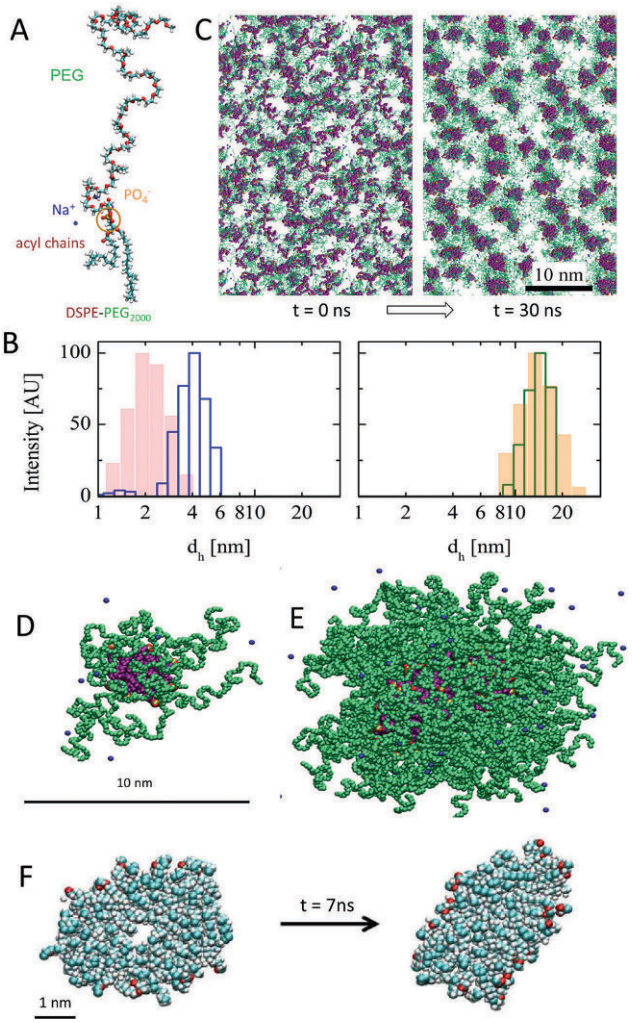


Fig. 1 Simulated self-assembly of DSPE-PEG_{2000} copolymers in water. (A) Atomistic structure of a relaxed DSPE-PEG_{2000} copolymer. (B) Experimental distribution of the observed sizes of DSPE-PEG_{2000} micelles self-assembled (left) in water and (right) in a 5 mM HEPES-buffered saline. Histograms of data from NICOMP (lines) and Brookhaven (shadow) dynamic light scattering instruments obtained at a 90° angle. (C) Snapshots of initial (0 ns) and final (30 ns) systems of DSPE-PEG_{2000} monomers in water. Hydrophobic and hydrophilic blocks are shown in purple and green. Simulated micelles in (D) water and (E) 0.16 m NaCl solution. (F) The hydrophobic core of the 90-monomer micelle in NaCl became ellipsoidal over the course of the 7 ns simulation. The size of a 90-monomer micelle shown in (E) and the shape of the core in (F) were used to validate the computational model of the micelle.[20] Reproduced from ref. 20 with permission from the American Chemical Society, copyright 2011.

The observed micelle size differences were clarified in atomistic MD simulations.[20] First, the formation of small DSPE-PEG_{2000} micelles in water was simulated. Initially, randomly distributed monomers at a concentration of c = 40 mM were solvated at T = 300 K in water. Within 30 ns, small micelles, with $N_{agg} < 11$, developed in the system, as shown in Fig. 1(C). These micelles had hydrophobic cores, ionic interfaces (charged monomers), and a semi-polar palisade PEG layers. Neighboring micelles



Petr Král

Prof. Petr Král received in 1986 a MSc degree at the Czech Technical University. In 1995, he received a PhD degree in theoretical condensed matter physics with Prof. Bedřich Velický at Czech Academy of Sciences (CAS). In 1996–2004, he held postdoctoral and visiting scientist positions at the Universities of Nottingham and Toronto, and the Weizmann Institute of Science, last one with Prof. Moshe Shapiro. In 2004, he joined the faculty of the Department of Chemistry at the University of Illinois at Chicago, where he became a full Professor in 2015. His current research is focused on simulations of nanomedicines, self-assembly of nanoparticles, nanofluidics, electronic structures and transport in nanostructures.

Published on 12 April 2018. Downloaded by University of Illinois at Chicago on 8/23/2018 9:50:25 PM.

often came in contact through their extended PEG coronas, but they did not grow further, despite the relatively large DSPE-PEG$_{2000}$ concentration. The micelles sizes matched the experiments (in water), revealing that the experimental micelles were formed by $N_{agg} \leq 8$ monomers,[20] as shown in Fig. 1(D).

In the saline solution, due to time limits, only one micelle with $N_{agg} = 90$ monomers was prepared and equilibrated, matching the data from small-angle neutron scattering measurements.[21] Fig. 1(E) shows the relaxed micelle, which had a diameter of $d \approx 14$ nm, in close agreement with dynamic light scattering experiments. Fig. 1(F) reveals that the micelle core departed from a spherical shape, giving an aspect ratio of ≈ 1.7. Experimentally, large micelles with $N_{agg} = 93$ present in saline solutions were observed to have oblate shapes.[21]

The simulations clearly revealed why micelles had different sizes in different solutions.[20] In these micelles, charged phosphate groups ($-PO_4^-$) form an interfacial region separating their hydrophobic core and PEG corona. The simulations revealed that the probability of finding Na^+ ions close to the $-PO_4^-$ groups is much larger in saline solutions than in pure water. At low ionic concentrations, the assembled $-PO_4^-$ groups are less screened and thus effectively larger (more repelling), making the monomers more "triangular" in shape, so that only smaller micelles can be formed. At higher ionic concentrations, the screened $-PO_4^-$ groups allow a more compact assembly, leading to larger micelles.

Further structural details of micelles can also be examined by modeling. Fig. 2 shows the distributions of hydrophobic and hydrophilic (PEG) groups of self-assembled DSPE-PEG$_{2000}$, as well as water, with a radial distance from the micelle centers. Small micelles assembled from 10 DSPE-PEG$_{2000}$ (SSM-10) in water have small hydrophobic cores and a sharp distribution of PEG, surrounded by water at nearly bulk density. Larger micelles assembled from 90 DSPE-PEG$_{2000}$ (SSM-90) in saline solution have larger hydrophobic cores, extended PEG layers and a gradually increasing water/ion concentration. Moreover, small micelles have a very uneven PEG corona, so that $\approx 30\%$ of the core is always fully exposed to water.[20] In the larger micelles, the PEG corona is relatively dense and several nanometers thick, with only $<10\%$ of hydrophobic cores being exposed to water.

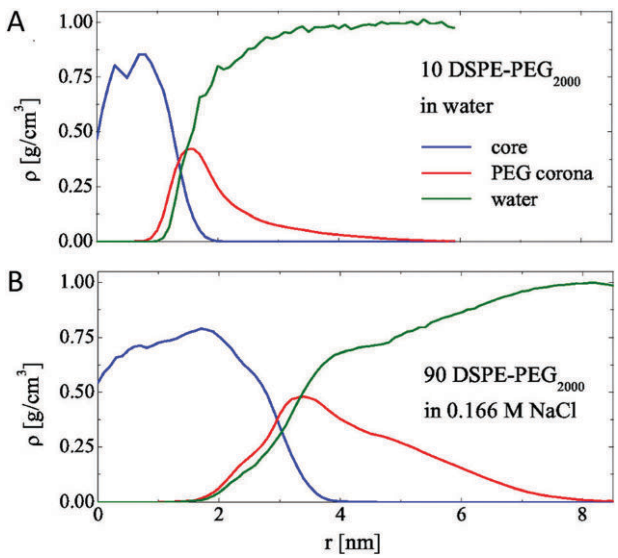


Fig. 2 Simulated density distributions of hydrophobic core groups, PEG groups and water for micelles in (A) water (SSM-10) and in (B) 0.16 M NaCl solution (SSM-90). Density of core and PEG corona of the micelle and density of water with a radial distance from the center of the micelle.[20] Reproduced from ref. 20 with permission from the American Chemical Society, copyright 2011.

4 Solvation of drugs in micelles

Atomistic simulations can clarify the number, the location and the binding strength of drugs that can be accommodated within the nanocarriers.[22–24] A reasonable agreement with experiments was also obtained by coarse-grained simulations of drug loading in micelles.[25] Such simulations could help to optimize accommodation, transport, and delivery of therapeutic agents in nanomedicines.

4.1 Solvation of small drugs in micelles

MD simulations were used to model solvation of drugs in micelles described above in Section 3.[26] In experiments, ≈ 11 bexarotene molecules were observed to solvate on average in micelles with 90 monomers (SSM-90) (Fig. 1(E)). Fig. 3(A) shows the Gibbs free energy profiles, $\Delta G(r)$, calculated for the amphiphilic bexarotene molecule along the radial coordinate r in SSM-10 (Fig. 1(D)) and SSM-90 (Fig. 1(E)).[20] In SSM-10, $\Delta G(r)$ has a single global minimum around $r = 1$ nm, while in SSM-90 two separated minima of different depths are observed around $r = 0.5$ nm (local) and $r = 2$ nm (global). Within the hydrophobic/hydrophilic interfacial minima, located between the alkane cores and the ionic interfaces at $r \approx 0.8$–1.2 nm (SSM-10) and $r \approx 1.7$–2.5 nm (SSM-90), bexarotene has its polar –COOH group oriented towards the aqueous region, while its body is

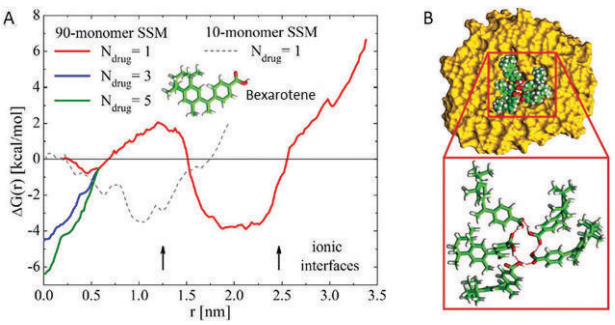


Fig. 3 (A) Free energy profiles of bexarotene in SSM-10 (water) and SSM-90 (0.16 M NaCl); SSM-10 and SSM-90 refer to micelles assembled from 10 and 90 monomers, respectively. Arrows show the positions of ionic interfaces in the two SSMs. (inset) The structure of bexarotene; the molecule contains carbon (green), oxygen (red) and hydrogen (white) atoms. (B) A snapshot of a 5 bexarotene molecules cluster formed inside the SSM-90 core after 11 ns of equilibration. A hydrogen bond network between –COOH groups is highlighted.[26] Reproduced from ref. 26 with permission from the American Chemical Society, copyright 2013.

 This journal is © The Royal Society of Chemistry 2018

Published on 12 April 2018. Downloaded by University of Illinois at Chicago on 8/23/2018 9:50:25 PM.

immersed in the alkane region. In both micelles, the barriers for transfer of bexarotene from these minima into the alkane cores are $\Delta\Delta G(r) \approx 4$ kcal mol^{-1}, whereas the barriers for its transfer into the aqueous PEG regions are $\Delta\Delta G(r) \approx 10$ kcal mol^{-1}.[26]

It is rather surprising that bexarotene doesn't have a global free energy minimum in the hydrophobic SSMs cores, considered to be the dominant residing region for poorly water-soluble drug molecules.[27] Fig. 3(A) shows that a single bexarotene has only a shallow local minimum in the SSM-90 collapsed core (Fig. 1(F)), where the energy necessary to form a cavity is decreased, due to a lower density of alkane tails.

To understand better how 11 bexarotene molecules might be stored in SSM-90, as observed in experiments, 3 and 5 drugs were also accommodated in the SSM-90 core. Fig. 3(B) shows that after $t \approx 11$ ns of equilibration 5 bexarotene molecules form a hydrogen bond network within the alkyl core. The drugs reorient into a configuration with inwards pointing –COOH groups, thus forming a molecular cluster held together by a hydrogen bond network (an analogue of a small inverse micelle). The observed clustering decreases the Gibbs free energy per molecule in the core, as shown in Fig. 3(A). The $\Delta G(r)$ depth increases with the number of drugs present in the core and for 5 drugs it surpasses the local minimum at the ionic interface, which can explain the large drug loading capacity of SSM-90.

4.2 Complexation of therapeutic peptides with micelles

Large therapeutic agents can also be carried by micelles.[28] In the next example, binding of a vasoactive intestinal peptide (VIP) to a micelle assembled from 20 monomers (SSM-20) in water is modeled.[26] The modeled VIP has a net charge of +3. It contains two clusters of positively charged residues (Arg-Leu-Arg-Lys and Lys-Lys), two well separated negatively charged residues (two Asp), and charged C and N termini.

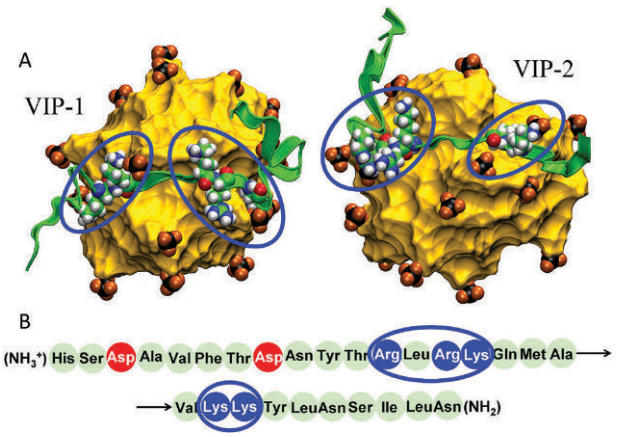


Fig. 4 (A) MD snapshots of VIP complexed in two distinct configurations (VIP-1, VIP-2) on the opposite sides of SSM-20. The alkyl core (yellow surface), is surrounded by PO_4^- groups (black, orange), which coordinate with two positively charged regions on each VIP. Whole VIP molecules are shown as green ribbons, and all the atoms of the positively charged residues are shown as spheres. (B) The amino acid sequence of VIP: neutral (light green), negative (red) and positive (blue).[26] Reproduced from ref. 26 with permission from the American Chemical Society, copyright 2013.

Initially, two VIP molecules were placed on the opposite sides of SSM-20, within 0.7 nm of its core edge, and the whole system was equilibrated for $t \approx 30$ ns. After the first ≈10 ns, both VIP molecules became closely coordinated to the PO_4^- groups positioned at the surface of the alkane core, as shown in Fig. 4. The PO_4^- groups migrated primarily towards the two clusters of positively charged residues, and redistributed more homogeneously on the alkane core surface. The coordination of PO_4^- groups with the positive residues of VIP occurs due to strong Coulombic coupling, which is poorly screened in water (Debye length in 1 mM PB solution is $\lambda_d \approx 9.7$ nm). The above modeling reveals how more complex molecules can be bound to micelles.

5 Dendron copolymer micelles

So far, micelles formed by linear block copolymers were discussed. An ideal copolymer should have a low critical micelle concentration, to remain assembled as a micelle upon dilution in a bloodstream, and a high hydrophilic–lipophilic balances, to have increased *in vivo* circulation times and reduced non-specific biological interactions. Micelles based on PEGylated dendron based copolymers (PDCs) have an improved stability, drug retention time, specificity, and other properties.

5.1 Structure and properties of dendron micelles

Recently, PDCs micelles were experimentally and computationally studied.[29–32] Fig. 5(A) shows the three components of PDCs: a poly-ε-caprolactone (PCL) hydrophobic core-forming block, a 2,2-bis(hydroxyl-methyl)propionic acid generation 3 (G3) dendron with an acetylene core, and PEG forming the hydrophilic coronna.[29] PDCs were synthesized and modeled with varying molecular weights for PCL and mPEG (3.5 and 14 kDa for PCL; 2 and 5 kDa for mPEG). The structures of individual PDCs and their micelles were compared to their linear block copolymer (LBC) counterparts having a similar hydrophilic–lipophilic balance. Fig. 5(B) illustrates that the experimental PDCs had significantly lower critical micelle concentrations compared to LBCs with similar hydrophilic lipophilic balance.

Fig. 5(C) illustrates the simulated structures of individual copolymers after 5 ns of equilibration in water at $T = 300$ K. PDCs (iii) maintained a more conical shape than LBCs (ii) with identical hydrophilic–lipophilic balances, due to the presence of G3-dendron keeping the PEG block closer to the PCL core. This pre-organization of multiple PEG blocks in PDCs (entropic cost) resulted in a more favorable micelle self-assembly (lower CMC). Fig. 5(D) shows three simulated micelles formed by 128 LBCs, 14 PDCs, and 10 PDCs. These simulations clearly illustrate that due to their more compact conical shapes, PDCs self-assemble into micelles with denser PEG layers and more complete surface coverage of the hydrophobic PCL core as compared to LBC micelles.

5.2 Multivalent coupling of micelles to cell membranes

In order to be able to deliver drugs, micellar nanocarriers need to specifically or non-specifically bind to cell membranes and

Published on 12 April 2018. Downloaded by University of Illinois at Chicago on 8/23/2018 9:50:25 PM.

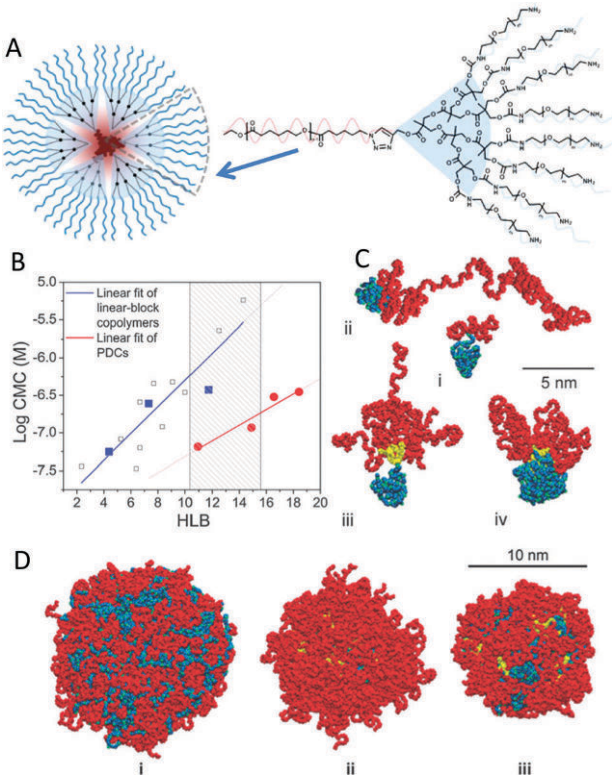


Fig. 5 Experimental and simulated results for linear and dendron micelles. (A) Scheme of a PDCs micelle formation. (B) The relationship between critical micelle concentration (CMC) and hydrophilic lipophilic balance (HLB) for PDCs and linear copolymers. (C) Single PDC and LBC copolymers: (i) PCL3.5k–mPEG2k, (ii) PCL3.5k–mPEG16k, (iii) PCL3.5k–G3–mPEG2k, and (iv) PCL14k–G3–mPEG2k simulated for 5 ns in water. (D) Simulated PDC and LBC micelles: (i) 128 PCL3.5k–mPEG2k, (ii) 14 PCL14k–G3–mPEG5k, and (iii) 10 PCL14k–G3–mPEG2k. PCL (blue), G3-dendron (yellow), PEG (red).[29] Reproduced from ref. 29 with permission from the Royal Society of Chemistry, copyright 2011.

pass drugs through them. Recent experiments have shown that neutral and negatively charged dendrimers (separate molecules) have a small non-specific coupling with cell membranes. However, positively charged dendrimers display a larger coupling with negatively charged cell-membranes, leading to their high toxicity.[33]

It was hypothesized that the surface functionality of PDCs micelles would also follow this trend, where positive surface charge would result in a highly non-specific cellular activity.[30] Therefore, PDCs were synthesized with PEG length 2000 and 3500 g mol^{-1}, functionalized with four different surface groups: amine (–NH_2), carboxyl (–COOH), acetyl (–$COCH_3$), and methoxy (–OMe). However, all four surface modified micelles yielded similar cellular uptakes and cell-associated fluorescence, so the amine-functionalized PDC micelles did not show an increased cellular activity, contrary to expectations.[30]

MD simulations were used to determine the cause of this lacking cellular activity. The two studied micelles had 15 PDCs composed of a G3 dendrimer with 8 PEG chains (600 and 2000 g mol^{-1} PEG) terminated with –NH_3^+ groups.[31] A lipid membrane consisting of dipalmitoylphosphatidycholine (DMPC) and dipalmitoylphosphatidylglycerol (DMPG) were used in a 3 : 1 ratio. The membrane was pre-equilibrated in ionic solution (150 mM NaCl). Then, these micelles were placed 5 Å above the membrane and the two systems were simulated for 75 ns.

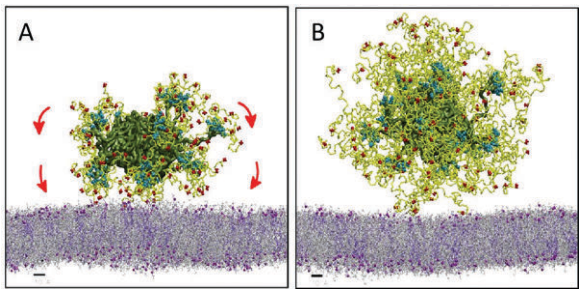


Fig. 6 Simulations (75 ns) of amine functionalized PDC micelles with different PEG chain lengths. (A) 600 g mol^{-1} PEG, (B) 2000 g mol^{-1} PEG length. PCL, G3-dendron (dark green), PEG chains (light green), amine terminus (red).[31] Scale bar is 1 nm. Reproduced from ref. 31 with permission from the American Chemical Society, copyright 2014.

After 30 ns, two PDCs were pulled away from the core of the PEG 600 micelle, and after 60 ns, this micelle began to spread and flatten over the membrane, as shown in Fig. 6(A). On the other hand, the PEG 2000 micelle did not bind significantly to the membrane and preserved its form, as shown in Fig. 6(B). The PEG 600 micelle spreading was a result of a multivalent binding of the amine groups to the negatively charged DMPG lipid molecules. The charged groups in PEG 600 chains acted more cooperatively, while the charged groups in the PEG 2000 chains acted more independently, without much affecting this micelle.

5.3 Target-specific binding of micelles to receptors

It is crucial to develop target-specific nanomedicines, since a non-specific delivery of drugs can lead to various side effects. Targeting ligands attached to nanocarriers can provide them with a specific binding to targets of interest. At the same time, PEG chains attached to nanomedicines can reduce the non-specific binding of nanocarriers.[34] However, a high density PEG may restrict the surface accessibility of targeting ligands.[35]

In recent experiments,[32] target-specific micelles were prepared by attaching targeting ligands (folic acid (FA) molecules) at the end of some PEG chains. It was hypothesized that stronger targeting interactions could be formed by decreasing the length of PEG chains (as in Fig. 6), increasing the number of targeting ligands, and increasing the clustering of targeting ligands.[32] Three different PEG chains (600 g mol^{-1}, 1000 g mol^{-1} and 2000 g mol^{-1}) were used in the experimental micelles. It turned out that decreasing the length of PEG chains, with some of them being functionalized by targeting ligands (FA), had almost no effect on the targeting strength of the micelles, while increasing the number of targeting ligands, and thus their clustering, caused in some cases even a reduction of this strength. A micelle with 5% of targeted PEG 2000 and 95% untargeted PEG 600 has shown the maximum enhancement of cellular interactions (25 fold stronger than untargeted PDCs). Eventually, it turned out that all three hypotheses raised above were incorrect.[32]

 This journal is © The Royal Society of Chemistry 2018

Published on 12 April 2018. Downloaded by University of Illinois at Chicago on 8/23/2018 9:50:25 PM.

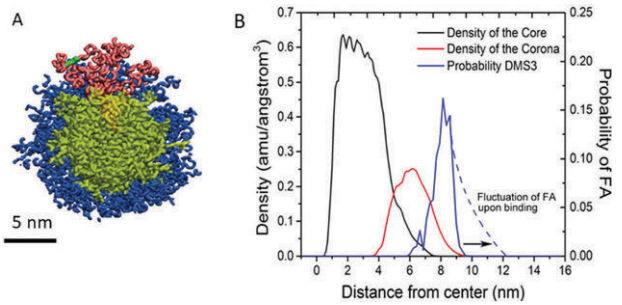


Fig. 7 (A) A simulated PEG_{600}/PEG_{2000}–FA (DMS3) micelle; PCL core (yellow), PEG (blue), PDC–FA (pink), FA (green). (B) Radial density distribution of the core and corona in DMS3 and a probability distribution of FA position with respect to the DMS3 micelle center.[32] Reproduced from ref. 32 with permission from the American Chemical Society, copyright 2016.

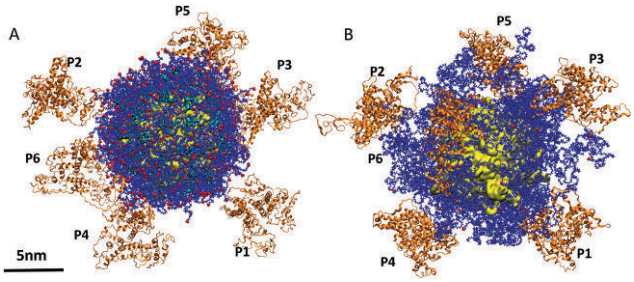


Fig. 8 Simulated (A) PDCs and (B) LBCs micelles interacting with six BSA proteins. Proteins (orange ribbons), PCL cores of the micelles (yellow surface), dendrimer of dendron micelle (cyan surface), PEG chains (blue) blue and terminal methyl groups (red).[38] Reproduced from ref. 38 with permission from the American Chemical Society, copyright 2014.

In order to clarify why certain mixed micelles show stronger targeted interactions, micelles containing 5% targeted PDCs were modeled by atomistic MD simulations: (DMS2) PEG 600 and PEG 600 with FA; (DMS3) PEG 600 and PEG 2000 with FA; (DMS7) PEG 1000 and PEG 2000 with FA; (DMS10) PEG 2000 and with PEG 2000 FA. Individual PDCs were assembled into micelles (aggregation number of 60) and equilibrated. Fig. 7(A) shows the strongest targeting micelle, DMS3, after 50 ns of simulations in a 150 mM NaCl solution.

The simulated systems were analyzed to determine the solvent accessible surface area (SASA) of their FA, the local PEG density near FA, and the distribution of FA positions with respect to the micelle center. The results have shown that all four systems had FA SASA within 400 ± 50 Å^2. The strongest targeting micelle (DMS3) had the lowest PEG density within 2 Å from FA, but no clear correlation was found between the local PEG density around FA and the micelle targeting strength. In most micelles, the calculated distributions have shown that FA was largely localized within the PEG corona, which was the likely reason for their reduced activity. However, in DMS3, the PEG surface was positioned 8.0 ± 0.5 Å from the micelle center, while the PEG chain containing FA could extend up to 12 Å, under proper binding conditions, as shown in Fig. 7(B). This was certainly not possible in DMS2 or DMS10, where the targeted PEG chains had the same length as the non-targeted PEG chains. The FA molecules also had the tendency to couple with each other at high FA concentrations, which could reduce their potential coupling with the receptors. Overall, the simulations have shown that in the DMS3 micelle, with the strongest binding to the target, FA had the largest conformational freedom.

5.4 Deleterious role of protein corona on micelles

One of the most important challenges affecting the performance of nanocarriers is their residual interaction with serum proteins. Despite the fact that PEG-ylated systems tend to interact very little with the serum, they can still be affected and even destabilized by these residual interactions.[36] Therefore, a poly(2-oxazoline)s polymer has been developed,[37] which can potentially make more robust drug nanocarriers than PEG.

It was also hypothesized that PDCs micelles can be more stable in the serum (longer life times) than LBCs micelles, due to their high surface densities of protecting chains and lower CMCs.[38] A drug release study with PEG-ylated PDCs and LBCs micelles indeed demonstrated a greater serum stability of the PDCs micelles. The average half lives of PCL3.5k–G3–8PEG600 and PCL3.5k–PEG5k micelles in 50% fetal bovine serum were 5.51 and 11.35 hours, respectively.

Atomistic MD simulations were performed to compare interactions of PEG-ylated PDCs and LBCs micelles with serum proteins.[38] The PDCs and LBCs micelles were formed by PCL3.5k–G3–8PEG600 and PCL3.5k–PEG5k polymer building blocks, respectively. Both micelles had the same terminal group ($-CH_3$) and the same number of monomers (60). BSA (bovine serum albumin), a main component of the blood serum, was chosen to separately interact with the PDCs and LBCs micelles. Six BSA proteins with different orientations were placed around each micelle in a 150 mM NaCl solution.

Fig. 8 displays the two micelle systems simulated for 20 ns. In the PDCs micelle (Fig. 8(A)), the relaxed PEG chains generate a smooth surface, providing a little room for strong BSAs coupling. On the other hand, in the LBCs micelle (Fig. 8(B)), the relaxed PEG chain form a highly diffuse PEG corona, which nests the BSA proteins. The LBCs micelle core is also less protected than that of a PDCs micelle, which allows its stronger binding to the serum proteins. The LBCs micelles can be destabilized for all the above reasons. In order to quantify this possibility, the BSA-micelle coupling energies were calculated and averaged over the six BSAs. The average (molecule and time) interaction energies of one BSA protein with PDCs and LBCs were -60.2 kcal mol^{-1} and -178.6 kcal mol^{-1}, respectively. Therefore, the average coupling energy of BSAs with the LBCs micelle was about 3 times larger. This can explain why LBCs micelles tend to be destabilized more in the serum.

6 Nanoparticles nanomedicines

Nanomedicines can not only act like suitable nanocarriers of drugs, but they can be designed to act alone like a large drug with a specific binding to relevant receptors. Here, few examples of modeling of such systems are discussed, starting with examples showing a general coupling of proteins to nanoparticles.

Published on 12 April 2018. Downloaded by University of Illinois at Chicago on 8/23/2018 9:50:25 PM.

6.1 Controlling proteins on nanoparticles

Recent experiments have shown that the conformations of proteins adsorbed on NPs surfaces can be controlled by the NPs charged ligands.[39] In order to explain these observations, the experimental systems were modeled by MD simulations. The model Au NPs (12 nm diameter) had either citrate or (16-mercaptohexadecyl)trimethylammonium bromide (MTAB) ligands, where only a fraction of ligands of the NPs were charged (shown in red and blue in Fig. 9). An α-synuclein protein was adsorbed on the ligated NPs. The systems were simulated for 50 ns in 20 mM NaCl aqueous solvent.

Fig. 9 shows typical conformations of α-synuclein adsorbed on both NPs, where the anionic citrate NP is Coulombically attracting the positive N-terminus (amino acid label 0) and repelling the negative C-terminus (amino acid label 140) of α-synuclein. Opposite interactions/conformations were found for the cationic MTAB NP. The average distances of all the amino acids from the closest NP ligands are shown on the simulation plots (Fig. 9). They agree with the NMR data shown on the experimental plots (Fig. 9). In both systems, interactions of charged ligands and adjacent oppositely charged amino acids effectively reduce the NMR signal strength.[39]

6.2 Super-enzymatic activity on nanoparticles surfaces

NPs might act like nanomedicines when certain biochemical reactions take part on their surfaces. For example, it was shown that proteolytic activities of enzymes can be significantly enhanced on surfaces of NPs.[40] In the experiments, ZnS NPs (diameter of 5 nm) with the following (200) ligands were prepared: neutral PEGylated (OMe), positive PEGylated (NH2), negative PEGylated zwitterionic (zwit) and short negative zwitterionic (CL4) ligands. The cleaved peptide (N-*CSTRIDEANQA ATSLP7SH6-COOH where Cy3 is attached to the cysteine thiol*) contains four modules within its sequence, (a) N-terminal cysteine thiol used for dye labeling, (b) the STRIDEANQAAT which contains trypsin recognizable arginine residue, trypsin cleaves its C-terminal side,[41] (c) the SLP7S forms a type II polyprolyl helix used as spacer to keep the peptide away from the QD surface,[42] (d) H6, used to attach the peptide with QD surface. The enzymatic efficiency was studied *via* the specificity constant k_{cat}/k_m, where k_{cat} is a turnover rate and k_m is the Michaelis constant. The efficiency was decreasing in this order: CL4 (35 times larger than freely diffusing peptide), Zwit (18 times larger), NH2 (12 times larger) and OMe (3.5 times larger).

It was hypothesized that mainly two parameters are responsible for the enhanced enzymatic activity: (a) the peptide exposure above the NPs ligand corona and (b) the strength of enzyme coupling to the NPs corona. Separate MD simulations were performed to test both hypothesizes. To evaluate the first parameter, four different NPs (OMe, NH2, Zwit and CL4) were prepared. Each NP (5 nm diameter core) had 200 homogeneously distributed ligands and 4 peptides attached through terminal hexahistidine residues to its core. The simulations were performed for 90–100 ns in 150 mM NaCl solution. Fig. 10(A) shows CL4 and OMe NPs with the 4 attached peptides. The solvent accessible surface area (SASA) of the peptides was calculated for each NP. Fig. 10(B) shows that peptides had the highest exposure in CL4 NP and the lowest exposure in OMe NP, which is fitting the experimental enzymatic activities.

The same NPs and simulation conditions were used in evaluation of the second parameter, except that only four trypsin enzymes were placed close to these NPs. Fig. 10(C) displays the

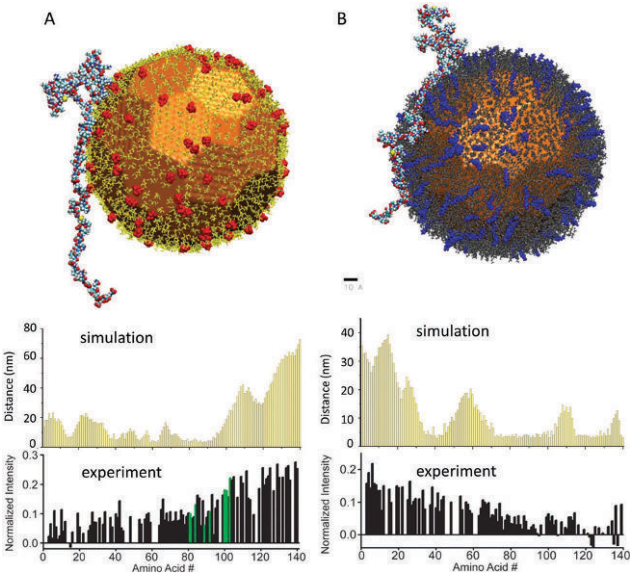


Fig. 9 Simulated gold NPs with (A) citrate and (B) MTAB ligands interacting with an α-synuclein protein; 10% of ligands were charged (red and blue) and other ligands were neutral (yellow and grey). Plots labeled "simulation" show the distance of amino acids from closest NP ligands. Plots labeled "experiment" show the normalized intensity of the amino acids in HSQC NMR experiment. The experiments and simulations are well correlated.[39] Reproduced from ref. 39 with permission from the American Chemical Society, copyright 2015.

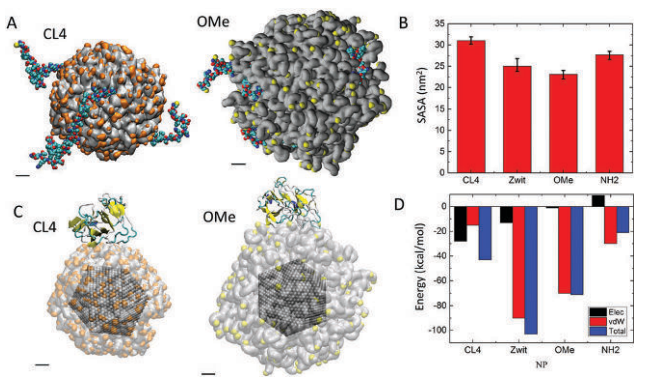


Fig. 10 Different NPs with attached peptides or adsorbed enzymes, simulated for 90 ns in a physiological salt concentration (150 mM). (A) Peptides attached to CL4 and OMe NPs; zwitterionic groups of CL4 (orange) and methoxy groups of OMe (yellow). (B) Exposed surface area of the peptides in nm^2 for CL4, Zwit, OMe and NH2 NPs. (C) CL4 and OMe NPs with an adsorbed trypsin enzyme. (D) The average interaction energy (electrostatics, vdW and total) between a trypsin enzyme and different NPs.[40] All the scale bars are 1 nm. Reproduced from ref. 40 with permission from the American Chemical Society, copyright 2017.

 This journal is © The Royal Society of Chemistry 2018

Published on 12 April 2018. Downloaded by University of Illinois at Chicago on 8/23/2018 9:50:25 PM.

enzymes configurations that have the strongest attachment to the chosen NPs. Fig. 10(D) shows the average interaction energies (electrostatics and van der Waals) for the enzyme configurations with the strongest binding with each NP, calculated using a dielectric constant of water (78.5). The enzymes had the strongest coupling with Zwit NP and the weakest with the positively charged NH2 NP (repulsion). For neutral NP, the electrostatic coupling was almost zero, but the van der Waals (vdW) coupling was relatively large (-70 kcal mol^{-1}). The enzyme interacted only in a specific orientation and for a short time with the positively charged NH2 NP. This explained why the kinetic enhancement was lower for NH2 than for Zwit, even though the exposure of peptide was higher for NH2. These simulations revealed that the kinetic activity of enzymes on NPs surfaces is controlled by a balance of multiple parameters.[40]

6.3 Deleterious coupling of nanoparticles to viruses

In recent pioneering studies, small gold NPs with predesigned ligand-covered surfaces were shown to disintegrate certain classes of viruses (human papillomavirus (HPV), dengue, herpes simplex virus (HSV)).[43] These viruses are known to start infecting cells by recognizing heparan sulfate proteoglycan molecules (HSPG) embedded in their membranes. The NPs were covered by mercaptoundecanesulfonate (MUS) ligands, mimicking HSPG, thus facilitating their faked recognition by the viruses. NPs covered with sulphonated but much shorted mercaptoethanesulfonate (MES) ligands or phosphonated mercaptoundecanephosphonate (MUP) ligands were not able to disintegrate the viruses.

In order to understand better these results, atomistic MD simulations were performed of the experimental NPs interacting with the capsids of HPV-16 and other viruses placed in a physiological solution (150 mM NaCl).[43] Initially, different NPs were placed close to the solvent-exposed HSPG binding sites (K278, K356, K361, K54, K59 (blue residues of Fig. 11(A))) of an HPV L1 pentamer protein.[43] Fig. 11(A) (left) shows the simulation results for MUS:OT NP (2.4 nm core with 50 MUS ligands and 50 octanethiol (OT) ligands). In the 50–80 ns simulations, 5–6 specific local interactions (multivalent binding) have been formed between the charged sulfonate groups of MUS:OT NP and the HSPG binding sites (lysine or arginine). Each of the sulfonate groups binds to lysine residues with a Gibbs free energy of -6 kcal mol^{-1},[44] totaling (whole NP) in -34 kcal mol^{-1}, while the non-polar ligand chains acquire on average a non-local total binding energy of -21 kcal mol^{-1}.[43] Considering the change of Coulombic free energy of binding with the NP changing distance, the applied force on L1 pentamers by each MUS:OT NP was estimated to be $F \approx 189$ pN.

Interactions of other experimental NPs with the HPV capsid were also simulated. For example, MUS NPs (2.4 nm core with 100 MUS ligands) behaved like MUS:OT in terms of multivalent attachment and local capsid deformations, but it took longer time before it nested on the L1 pentamer. Fig. 11(A) (middle) also shows the results for MES1 NP (2.4 nm core with 100 MES ligands), which only hops on the L1 pentamer, whereas MES2 (4 nm core and 250 MES ligands) occasionally binds to 1–2 lysine residues. However, neither MES1 nor MES2 can be

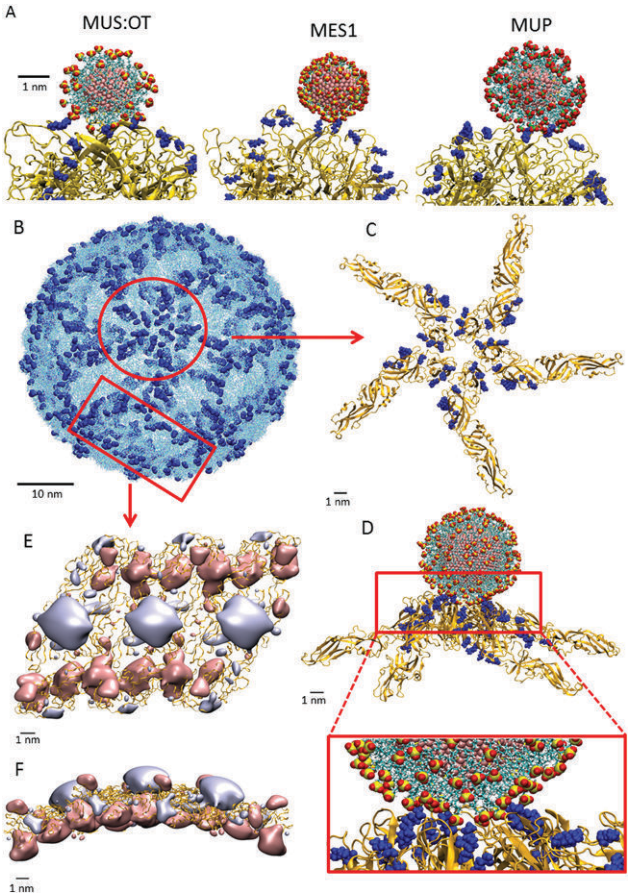


Fig. 11 Simulations of NPs coupled with a viral capsid (HPV) and envelope proteins (dengue virus). (A) Side view of the interactions of MUS:OT, MES1 and MUP NPs with a HPV L1 pentamer, with highlighted positively charged HSPG binding residues (K278, K356, K361, K54, K59 – blue). (B) Whole envelope proteins of a dengue virus with shown residues of the HSPG binding sites (blue).[45] Selected regions of dengue envelope proteins are highlighted (red areas). (C) Star-like protein arrangement having at the center a high concentration of HSPG residues. (D) Side view of MUS:OT NP interacting with HSPG binding sites after 10 ns of simulations. (inset) A magnified view of the coupling. (E and F) Top and side views of electrostatic surfaces of a leaf-like segment. Negative (−2.3 V – pink) and positive equipotential (2.3 V – light blue) surfaces, respectively.[43] Reproduced from ref. 43 with permission from the Springer Nature, copyright 2017.

properly nested on the L1 pentamer to deform it. Finally, Fig. 11(A) (right) shows the results for MUP NP (2.4 nm core with 100 MUP ligands). Its phosphonate ligands self-interacted and formed clusters (HPO_3^- groups form H-bonds with each other), which could explain why MUP NP does not neutralize viruses in experiments (similar to MES1 and MES2).

Coupling of NPs to a dengue virus was also modeled as a part of the above studies.[43] Before entering into the host cell, viral envelope glycoproteins of a dengue virus bind to the HSPG molecules within the cell membrane. In the simulations, five proteins (1*p*58 pdb)[46] forming a star were extracted from the dengue envelope, as shown in Fig. 11(B and C). Initially, a MUS:OT NP (5 nm core, 180 MUS, and 180 OT ligands) was placed close to the central part of the star region, which contained many positively charged lysine and arginine HSPG-binding residues

Published on 12 April 2018. Downloaded by University of Illinois at Chicago on 8/23/2018 9:50:25 PM.

(K305, K307, K310, K295, K291, R288, R286, R188, K388, K393 and K394).[45] Within 20 ns, the number of selective Coulombic contact points between the NP and the protein complex was gradually increasing (Fig. 11(D)), in a full analogy to the HPV case (Fig. 11(A) (left)). Fig. 11(E and F) show that the elongated region between the star pentamers is also highly positive at its exterior and negatively charged at its interior. Over the time, these positive regions might be wrapped on the negatively charged MUS:OT NPs, thus helping to destabilize the virus. Therefore, the experimentally observed NP-destabilization of dengue and HPV viruses might be caused by similar mechanisms, except that the viral envelope is destabilized in a dengue virus rather than its capsid (HPV).

6.4 Coupling of nanoparticles to amyloid fibrils

Predesigned NPs might be able to affect other bio-molecular complexes, such as amyloid fibrils. Many experimental studies have investigated the inhibition of Aβ40 peptides self-assembly using polyphenol, quinone–tryptophan hybrid (NQTrp), and even NPs coated with histidine-based polymers.[47]

Here, MD simulations are presented of predesigned NPs interacting with self-assembled amyloid peptide fibrils, with to goal to destabilize them or block their further growth.[48] The used ligands were: positive (NH_3^+ terminal group), negative (SO_3^- terminal group), neutral (NQTrp terminal group) – all attached to PEG chains, and positive Cys-Glu-Leu-Val-Phe-Phe-Ala-Lys-Lys peptides (complementary sequence to that found in peptides forming the exposed part of a β-sheet surface (Aβ40)). Five different NPs (2.2 nm core) were simulated with these ligands: Pos (90 positive), PosNQ (80 positive and 10 neutral), NegNQ (80 negative and 10 neutral), Janus (45 positive and 45 negative) and Pep (90 peptide). Initially, these five NPs were separately placed 5–10 Å above the β sheet surface or at the fibril end, and the systems were simulated for ≈100 ns in a 150 mM NaCl solution.

Fig. 12(A) shows these NPs stabilized on the surface and tip of β sheet fibrils (Aβ40) after 90–95 ns of simulations. The obtained results show that Pos, PosNQ, Pep and Janus bind to the fibril sheet, but they do not bind to its end, while NegNQ does exactly the opposite: Pos interacts mainly with the negatively charged Glu22 amino acids, which gives a large contribution to its binding energy (Fig. 12(B)). In PosNQ, the positive ligands act like in Pos, but the neutral ligands are in contact with Hse14, Gln15, Lys16, Leu17, Val18, Phe20, Val24, Gly25, Ser26 and Asn27, which significantly increases the vdW contribution to the binding energy. Pep is mainly nested on Glu22, since it is positively charged, but the Coulombic and vdW contributions to its binding energy are similar. The coupling energy of Janus is small, since both ligands interact with oppositely charged amino acids; negatively and positively charged ligands mainly interact with Lys16 and Glu22, respectively. The attached NPs increase the average twist angle of the adjacent peptides in the fibril layer. The negatively charged NegNQ binds to the fibril tip and thus potentially block the fibril growth.

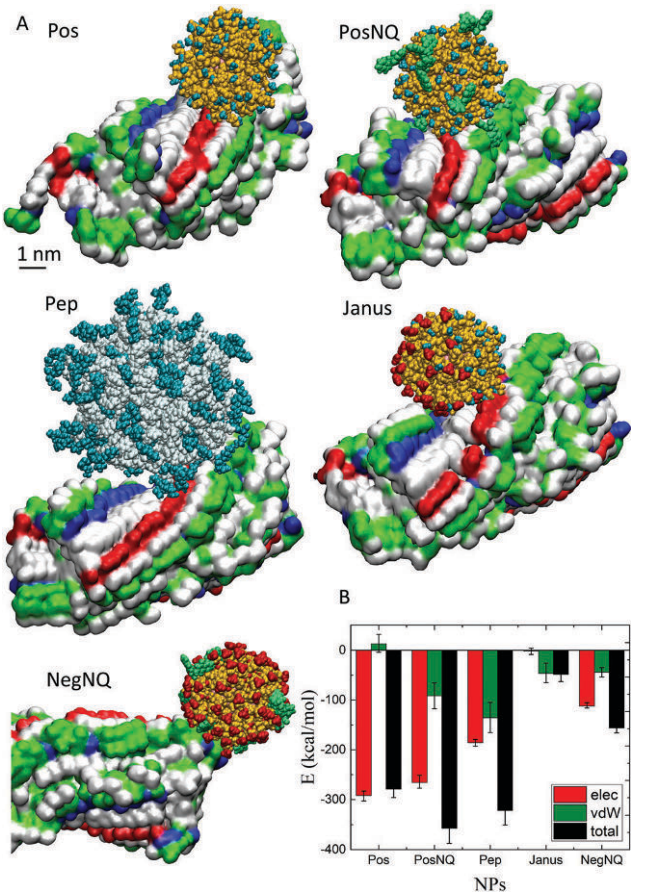


Fig. 12 (A) Simulations of NPs adsorbed on a Aβ40 fibril after 90–95 ns of equilibration. Positive amino acids (blue), negative amino acid (red), polar amino acid (green) and nonpolar amino acid (white). PEG chain (yellow), NH_3^+ (blue), SO_3^- (red) and NQTrp (green). (B) Binding energies of NPs to Aβ40 fibril.[48]

6.5 Biologically active organomimetic nanoclusters

Since gold NPs with ligands attached by thiolated groups are not particularly stable, organomimetic nanoclusters (OCNs) were developed by attaching selected ligands through a covalent perfluoroaryl linkage to small B_{12}^{2-} clusters.[49] In principle, OCNs could be designed to form highly specific and stable nanomedicines. In order to better understand the structures and activities of selected experimentally studied OCNs, MD simulations were used as before. Fig. 13(A and B) show selected OCNs with 12 ligands based on 16 PEG units, simulated in water for 30 ns. Their radius of gyration of $R_g \approx 3$ nm in both water and 80 mM PBS buffer solution at pH 7.4 was in a reasonable agreement with experiments.

To perform realistic experimental studies of a selective coupling of OCNs to chosen biological complexes, OCNs were coated with β-D-glucose ligands (Fig. 13(E) (left)) and such "sugar particles" (SPs) were let to couple with a natural concanavalin A (ConA). These SPs have shown a 6500 larger binding affinity to ConA as compared to free saccharides. Fig. 13(C) shows a simulation snapshot of this system, which revealed that SPs developed in 25 ns a highly stable multivalent

 This journal is © The Royal Society of Chemistry 2018

Published on 12 April 2018. Downloaded by University of Illinois at Chicago on 8/23/2018 9:50:25 PM.

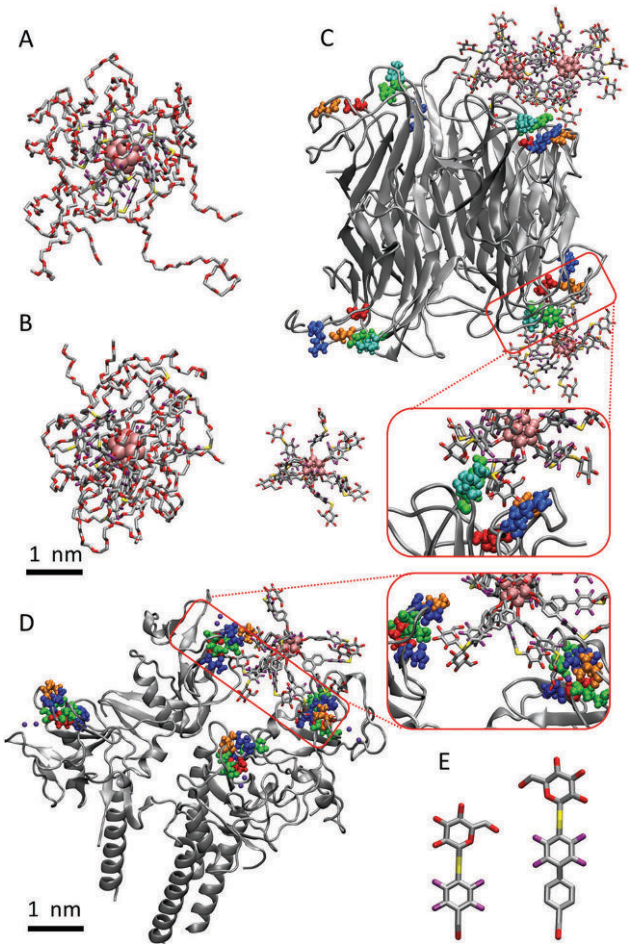


Fig. 13 (A) MD simulations of OCNs in water. Each OCN contains B_{12}^{2-} units. The core is attached with perfluoroaryl groups with ethereal linkage. The aryl groups are connected with PEG chains (16 ethylene glycol units). (B) The ligands of this OCN contains an extra benzyl group in between ether and perfluoroaryl group. (C) Simulated systems of tetramer protein concanavalin A and sugar-coated OCNs. (inset) Detail of a carbohydrate binding site (Asp (orange), Arg (blue), Leu (cyan), Tyr (green) and Thr (red)). (D) Simulation of another sugar-coated OCN with DC-SIGN protein which has a role in HIV infection. (inset) Detail like in (C). (E) Left and right ligands are used in (C) and (D) sugar coated OCNs respectively (carbon (gray), oxygen (red), sulfur (yellow), fluorine (purple)).[49] Reproduced from ref. 49 with permission from the Springer Nature, copyright 2016.

coupling to ConA tetramer (150 mM NaCl solution). At any moment, some SPs ligands interacted with ConA monosaccharide binding sites, formed by Asn14, Leu99, Tyr100, Asp208 and Arg228 residues. This multivalent binding of SPs was maintained by an effectively increased concentration of its β-D-glucose ligands on the SPs surfaces. In contrast, binding of a free β-D-glucose to the ConA tetramer is short and separated by long non-binding periods.

Another example of OCNs potential usage is based on DC-SIGN membrane proteins, which play an important role in a cellular internalization of HIV viruses.[50] The coupling of SPs with DC-SIGN was modeled to find out if SPs can inhibit DC-SIGN and HIV binding by blocking relevant carbohydrate binding sites in the protein. It was found that SPs with a shorter ligand (Fig. 13(E) (left)) can only interact with one carbohydrate binding site, while SPs with longer ligands (right) can be bound with two sites at the same time (Fig. 13(D)). This multivalent binding increases the binding affinity of SPs to DC-SIGN, which might inhibit its binding with HIV.

7 Conclusion

We have presented numerous examples of a precise modeling of nanomedicines performed by classical atomistic molecular dynamics simulations. By discussing nanomedicines based on nanocarriers and individual bio-active nanoparticles, we have clearly illustrated that precise modeling could be highly beneficial for the understanding of phenomena taking part in these important systems, which are currently being rapidly developed. Atomistic simulations can describe in great details the structures, various characteristics and activities of nanomedicines. They can reveal locations where drugs are carried, show how stable they are in their binding sites, and evaluate how nanomedicines interact with lipid membranes, receptors and other biological molecules, which can affect their stability. In the case of individual nanoparticles, precise simulations can capture the detailed nature of their coupling with biological components, such as peptides, proteins, their complexes (fibrils, viruses), and reveal how nanoparticles can modify the activity of such biological systems. The discussed examples show that precise modeling can be of large help during the development and optimization of novel nanomedicines when it is closely correlated with ongoing experimental studies.

Conflicts of interest

There are no conflicts to declare.

Acknowledgements

P. K. was supported by the NSF DMR-1506886 grant. L. V. was supported by startup funding from UTEP.

References

1 B. A. Chabner, *Cancer Chemotherapy: Principles and Practice*, Humana Press, Philadelphia, 1990.
2 N. Wiradharma, Y. Zhang, S. Venkataraman, J. L. Hedrick and Y. Y. Yang, *Nano Today*, 2009, **4**, 302–317.
3 L. E. van Vlerken, T. K. Vyas and M. M. Amiji, *Pharm. Res.*, 2007, **24**, 1405–1414.
4 S. Mura, J. Nicolas and P. Couvreur, *Nat. Mater.*, 2013, **12**, 991–1003.
5 M. Shao, Z. Hussain, H. E. Thu, S. Khan, H. Katas, T. A. Ahmed, M. Tripathy, J. Leng, H.-L. Qin and S. N. A. Bukhari, *Colloids Surf., B*, 2016, **147**, 475–491.
6 N. Nishiyama and K. Kataoka, *Pharmacol. Ther.*, 2006, **112**, 630–648.
7 J. N. Israelachvili, *Intermolecular and Surface Forces: With Applications to Colloidal and Biological Systems (Colloid Science)*, 1992.

Published on 12 April 2018. Downloaded by University of Illinois at Chicago on 8/23/2018 9:50:25 PM.

8 R. M. Sawant, J. P. Hurley, S. Salmaso, A. Kale, E. Tolcheva, T. S. Levchenko and V. P. Torchilin, *Bioconjugate Chem.*, 2006, **17**, 943–949.
9 V. P. Torchilin, *Pharm. Res.*, 2006, **24**, 1.
10 S.-G. Kang, G. Zhou, P. Yang, Y. Liu, B. Sun, T. Huynh, H. Meng, L. Zhao, G. Xing, C. Chen, Y. Zhao and R. Zhou, *Proc. Natl. Acad. Sci. U. S. A.*, 2012, **109**, 15431–15436.
11 S. Abel, F.-Y. Dupradeau and M. Marchi, *J. Chem. Theory Comput.*, 2012, **8**, 4610–4623.
12 J. A. Nash, A. L. Kwansa, J. S. Peerless, H. S. Kim and Y. G. Yingling, *Bioconjugate Chem.*, 2017, **28**, 3–10.
13 M. Kang, D. Lam, D. E. Discher and S. M. Loverde, Molecular Modeling for Micellar Drug Delivery, in *Computational Pharmaceutics: Application of Molecular Modeling in Drug Delivery*, ed. D. Ouyang and S. C. Smith, John Wiley & Sons, 2015, p. 53.
14 W. Humphrey, A. Dalke and K. Schulten, *J. Mol. Graphics*, 1996, **14**, 33–38.
15 J. C. Phillips, R. Braun, W. Wang, J. Gumbart, E. Tajkhorshid, E. Villa, C. Chipot, R. D. Skeel, L. Kale and K. Schulten, *J. Comput. Chem.*, 2005, **26**, 1781–1802.
16 K. Vanommeslaeghe, E. Hatcher, C. Acharya, S. Kundu, S. Zhong, J. Shim, E. Darian, O. Guvench, P. Lopes, I. Vorobyov and A. D. Mackerell, *J. Comput. Chem.*, 2010, **31**, 671–690.
17 C. G. Mayne, J. Saam, K. Schulten, E. Tajkhorshid and J. C. Gumbart, *J. Comput. Chem.*, 2013, **34**, 2757–2770.
18 S. J. Marrink, D. P. Tieleman and A. E. Mark, *J. Phys. Chem. B*, 2000, **104**, 12165–12173.
19 H. Cesur, I. Rubinstein, A. Pai and H. Önyüksel, *J. Nanomed. Nanotechnol.*, 2009, **5**, 178–183.
20 L. Vuković, F. A. Khatib, S. P. Drake, A. Madriaga, K. S. Brandenburg, P. Král and H. Onyuksel, *J. Am. Chem. Soc.*, 2011, **133**, 13481–13488.
21 L. Arleth, B. Ashok, H. Onyuksel, P. Thiyagarajan, J. Jacob and R. P. Hjelm, *Langmuir*, 2005, **21**, 3279–3290.
22 D. Sutton, S. Wang, N. Nasongkla, J. Gao and E. E. Dormidontova, *Exp. Biol. Med.*, 2007, **232**, 1090–1099.
23 X.-Y. Wang, L. Zhang, X.-H. Wei and Q. Wang, *Biomaterials*, 2013, **34**, 1843–1851.
24 J. Lim, S.-T. Lo, S. Hill, G. M. Pavan, X. Sun and E. E. Simanek, *Mol. Pharmaceutics*, 2012, **9**, 404–412.
25 J. Hao, Y. Cheng, R. J. K. U. Ranatunga, S. Senevirathne, M. C. Biewer, S. O. Nielsen, Q. Wang and M. C. Stefan, *Macromolecules*, 2013, **46**, 4829–4838.
26 L. Vuković, A. Madriaga, A. Kuzmis, A. Banerjee, A. Tang, K. Tao, N. Shah, P. Král and H. Onyuksel, *Langmuir*, 2013, **29**, 15747–15754.
27 S. B. Lim, A. Banerjee and H. Önyüksel, *J. Controlled Release*, 2012, **163**, 34–45.
28 A. Dagar, A. Kuzmis, I. Rubinstein, M. Sekosan and H. Onyuksel, *Drug Delivery Transl. Res.*, 2012, **2**, 454–462.
29 J. W. Bae, R. M. Pearson, N. Patra, S. Sunoqrot, L. Vuković, P. Král and S. Hong, *Chem. Commun.*, 2011, **47**, 10302–10304.
30 R. M. Pearson, N. Patra, H.-J. Hsu, S. Uddin, P. Král and S. Hong, *ACS Macro Lett.*, 2012, **2**, 77–81.
31 H.-J. Hsu, S. Sen, R. M. Pearson, S. Uddin, P. Král and S. Hong, *Macromolecules*, 2014, **47**, 6911–6918.
32 R. M. Pearson, S. Sen, H.-J. Hsu, M. Pasko, M. Gaske, P. Král and S. Hong, *ACS Nano*, 2016, **10**, 6905–6914.
33 P. R. Leroueil, S. A. Berry, K. Duthie, G. Han, V. M. Rotello, D. Q. McNerny, J. R. Baker, B. G. Orr and M. M. Banaszak Holl, *Nano Lett.*, 2008, **8**, 420–424.
34 J. L. Perry, K. G. Reuter, M. P. Kai, K. P. Herlihy, S. W. Jones, J. C. Luft, M. Napier, J. E. Bear and J. M. DeSimone, *Nano Lett.*, 2012, **12**, 5304–5310.
35 S. Hak, E. Helgesen, H. H. Hektoen, E. M. Huuse, P. A. Jarzyna, W. J. Mulder, O. Haraldseth and C. d. L. Davies, *ACS Nano*, 2012, **6**, 5648–5658.
36 J. Wu, Z. Wang, W. Lin and S. Chen, *Acta Biomater.*, 2013, **9**, 6414–6420.
37 O. Sedlacek, B. D. Monnery, S. K. Filippov, R. Hoogenboom and M. Hruby, *Macromol. Rapid Commun.*, 2012, **33**, 1648–1662.
38 H.-J. Hsu, Y. Han, M. Cheong, P. Král and S. Hong, unpublished.
39 W. Lin, T. Insley, M. D. Tuttle, L. Zhu, D. A. Berthold, P. Král, C. M. Rienstra and C. J. Murphy, *J. Phys. Chem. C*, 2015, **119**, 21035–21043.
40 S. A. Diaz, S. Sen, K. Boeneman Gemmill, C. W. Brown, E. Oh, K. Susumu, M. H. Stewart, J. C. Breger, G. Lasarte Aragones, L. D. Field, J. R. Deschamps, P. Král and I. L. Medintz, *ACS Nano*, 2017, **11**, 5884–5896.
41 W. R. Algar, A. Malonoski, J. R. Deschamps, J. B. Blanco-Canosa, K. Susumu, M. H. Stewart, B. J. Johnson, P. E. Dawson and I. L. Medintz, *Nano Lett.*, 2012, **12**, 3793–3802.
42 K. B. Gemmill, S. A. Diaz, J. B. Blanco-Canosa, J. R. Deschamps, T. Pons, H.-W. Liu, A. Deniz, J. Melinger, E. Oh, K. Susumu, M. H. Stewart, D. A. Hastman, S. H. North, J. B. Delehanty, P. E. Dawson and I. L. Medintz, *Chem. Mater.*, 2015, **27**, 6222–6237.
43 V. Cagno, P. Andreozzi, M. D'Alicarnasso, P. J. Silva, M. Mueller, M. Galloux, R. Le Goffic, S. T. Jones, M. Vallino, J. Hodek, J. Weber, S. Sen, E.-R. Janeček, A. Bekdemir, B. Sanavio, C. Martinelli, M. Donalisio, M.-A. Rameix Welti, J.-F. Eleouet, Y. Han, L. Kaiser, L. Vuković, C. Tapparel, P. Král, S. Krol, D. Lembo and F. Stellacci, *Nat. Mater.*, 2018, **17**, 195–203.
44 D. Matulis and R. Lovrien, *Biophys. J.*, 1998, **74**, 422–429.
45 Y. Chen, T. Maguire, R. E. Hileman, J. R. Fromm, J. D. Esko, R. J. Linhardt and R. M. Marks, *Nat. Med.*, 1997, **3**, 866–871.
46 W. Zhang, P. R. Chipman, J. Corver, P. R. Johnson, Y. Zhang, S. Mukhopadhyay, T. S. Baker, J. H. Strauss, M. G. Rossmann and R. J. Kuhn, *Nat. Struct. Biol.*, 2003, **10**, 907–912.
47 Y. Porat, A. Abramowitz and E. Gazit, *Chem. Biol. Drug Des.*, 2006, **67**, 27–37.
48 S. Sen, L. Vuković and P. Král, unpublished.
49 E. A. Qian, A. I. Wixtrom, J. C. Axtell, A. Saebi, D. Jung, P. Rehak, Y. Han, E. H. Moully, D. Mosallaei, S. Chow, M. S. Messina, J. Y. Wang, A. T. Royappa, A. L. Rheingold, H. D. Maynard, P. Král and A. M. Spokoyny, *Nat. Chem.*, 2016, **9**, 333–340.
50 C. M. Coleman, C. St. Gelais and L. Wu, *Adv. Exp. Med. Biol.*, 2013, **762**, 109–130.

 This journal is © The Royal Society of Chemistry 2018